

PAPER

# Beamforming effects on generalized Nakagami imaging

To cite this article: Xue Yu *et al* 2015 *Phys. Med. Biol.* **60** 7513

View the [article online](#) for updates and enhancements.

## Related content

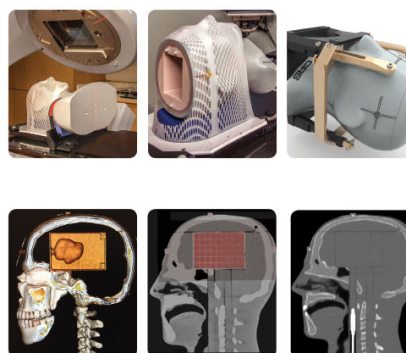
- [Classification of breast masses by ultrasonic Nakagami imaging: a feasibility study](#)  
Po-Hsiang Tsui, Chih-Kuang Yeh, Chien-Cheng Chang *et al.*
- [Three-dimensional ultrasonic Nakagami imaging for tissue characterization](#)  
Po-Hsiang Tsui, Cheng-Wei Hsu, Ming-Chih Ho *et al.*
- [Effect of logarithmic compression on estimation of the Nakagami parameter](#)  
Po-Hsiang Tsui, Shyh-Hau Wang and Chih-Chung Huang

## Recent citations

- [Ultrasound parametric imaging of hepatic steatosis using the homodyned-K distribution: An animal study](#)  
Jui Fang *et al*
- [Ultrasound window-modulated compounding Nakagami imaging: Resolution improvement and computational acceleration for liver characterization](#)  
Hsiang-Yang Ma *et al*
- [Acoustic structure quantification by using ultrasound Nakagami imaging for assessing liver fibrosis](#)  
Po-Hsiang Tsui *et al*

**High Fidelity** Simulation for Your SRS Program

**STEEV**  
STEREOTACTIC END-TO-END VERIFICATION



**CIRS**

# Beamforming effects on generalized Nakagami imaging

Xue Yu<sup>1</sup>, Yuexin Guo<sup>1</sup>, Sheng-Min Huang<sup>2</sup>, Meng-Lin Li<sup>2,3</sup> and Wei-Ning Lee<sup>1,4</sup>

<sup>1</sup> Department of Electrical and Electronic Engineering, The University of Hong Kong, Pokfulam, Hong Kong

<sup>2</sup> Department of Electrical Engineering, National Tsing Hua University, Hsinchu, Taiwan

<sup>3</sup> Institute of Photonics Technologies, National Tsing Hua University, Hsinchu, Taiwan

<sup>4</sup> Medical Engineering Programme, The University of Hong Kong, Pokfulam, Hong Kong

E-mail: [wnlee@eee.hku.hk](mailto:wnlee@eee.hku.hk)

Received 18 February 2015, revised 22 July 2015

Accepted for publication 24 July 2015

Published 15 September 2015



CrossMark

## Abstract

Ultrasound tissue characterization is crucial for the detection of tissue abnormalities. Since the statistics of the backscattered ultrasound signals strongly depend on density and spatial arrangement of local scatterers, appropriate modeling of the backscattered signals may be capable of providing unique physiological information on local tissue properties. Among various techniques, the Nakagami imaging, realized in a window-based estimation scheme, has a good performance in assessing different scatterer statistics in tissues. However, inconsistent  $m$  values have been reported in literature and obtained only from a local tissue region, abating the reliability of Nakagami imaging in tissue characterization. The discrepancies in  $m$  values in relevant literature may stem from the nonuniformity of the ultrasound image resolution, which is often neglected. We therefore hypothesized that window-based Nakagami  $m$  estimation was highly associated with the regional spatial resolution of ultrasound imaging. To test this hypothesis, our study investigated the effect of beamforming methods, including synthetic aperture (SA), coherent plane wave compounding (CPWC), multi-focusing (MF), and single-focusing (SF), on window-based  $m$  parameter estimation from the perspective of the resolution cell. The statistics of  $m$  parameter distribution as a function of imaging depth were characterized by their mean, variance, and skewness. The phantom with a low scatterer density (16 scatterers  $\text{mm}^{-3}$ ) had significantly lower  $m$  values compared to the ones with high scatterer densities (32 and 64 scatterers  $\text{mm}^{-3}$ ). Results from the homogeneous phantom with

64 scatterers  $\text{mm}^{-3}$  showed that SA, MF, and CPWC had relatively uniform lateral resolutions compared to SF and thus relatively constant  $m$  estimates at different imaging depths. Our findings suggest that an ultrasound imaging regime exhibiting invariant spatial resolution throughout the entire imaging field of view would be the most appropriate for Nakagami imaging for tissue characterization.

**Keywords:** backscattering, beamforming, Nakagami distribution, tissue characterization, ultrasound

(Some figures may appear in colour only in the online journal)

## Introduction

Tissue characterization is crucial for determining tissue types and its pathological states and distinguishing impaired tissue regions from normal ones in clinical practice. Noninvasive ultrasound-based tissue characterization methods can nowadays be classified primarily into parametric imaging and elastography (Ophir *et al* 1999, Thijssen 2002, Wells and Liang 2011, Mamou and Oelze 2013). These techniques collectively have been applied in various organs and tissues, for example, breast (Shankar *et al* 1993, Cespedes *et al* 1993, Bercoff *et al* 2004), myocardium (Miller *et al* 1985, Milunski *et al* 1989, Vered *et al* 1989, Konofagou *et al* 2002), liver (Kuc 1980, Ophir *et al* 1996, Sandrin *et al* 2003), and prostate (Feleppa *et al* 1996, Lizzi *et al* 1997, Salomon *et al* 2008). Conventional analyses on received radio-frequency (RF), envelope-detected or brightness mode (B-mode) ultrasound signals are performed to yield quantities that may be linked to tissue properties, such as scatterer density or microstructure (Mimbs *et al* 1981, Lizzi *et al* 1987, Insana *et al* 1991, Shankar 2000). Since the scattering behavior of small particles in tissues depends on the scattering cross section, number density, and arrangement patterns of scatterers (Wagner *et al* 1987, Tuthill *et al* 1988, Chen *et al* 1994a, 1994b, Shankar 2000, Oelze *et al* 2002, Tsui and Chang 2007), analyses on the backscattered echoes may provide additional information on local tissue properties.

Various models have been employed to describe the statistics of the envelope of the backscattered signals, which can generally be categorized into three conditions: Rayleigh, post-Rayleigh, and pre-Rayleigh distributions (Shankar 2000). When there is a large number (more than 10) of randomly distributed scatterers, whose size is much smaller than the ultrasound wavelength, in a resolution cell, the statistics of the backscattered envelope are Rayleigh (Szabo 2004). An example of the Rayleigh distribution can be observed in the blood pool on echocardiography (Nillesen *et al* 2008) and the normal liver (Molthen *et al* 1998). In addition to a large number of randomly spaced scatterers, regularly arranged scatterers are present in the resolution cell, resulting in the statistics of the envelope amplitude following the post-Rayleigh distribution (Shankar 2000). The post-Rayleigh distribution has been observed in liver fibrosis in a rat model (Ho *et al* 2012). In contrast, when there is only a small number of randomly spaced scatterers in a resolution cell, the statistics of the backscattered envelope fall in the pre-Rayleigh regime (Szabo 2004). An example of the pre-Rayleigh distribution is the myocardium on echocardiography (Nillesen *et al* 2008). The Rayleigh distribution is the earliest one proposed to model the statistics of the envelope of the backscattered ultrasonic echoes from soft tissues (Burckhardt 1978, Wagner *et al* 1983). The scattering behavior of biological tissues, however, cannot always be elucidated by the Rayleigh distribution, so more generalized models, including K, generalized K, homodyned K, and Nakagami distributions,

have been proposed to describe the ultrasound envelope statistics (Dutt and Greenleaf 1994, Shankar 1995). A systematic review (Destrempes and Cloutier 2010) on modeling of ultrasound echo envelopes in the case of a vanishing diffuse signal has shown that the homodyned K distribution is the best to model the real ultrasonic signals. Nevertheless, the inherent complexity of computing homodyned K distribution limits its application.

Nakagami distribution, on the other hand, has been demonstrated a good approximation of the homodyned K distribution (Destrempes and Cloutier 2010). Nakagami distribution, previously applied in radar (Nakagami 1960), has been shown capable of describing the ultrasound backscattered signals in biological tissues (Shankar 2000). It is a generalized two-parameter backscattering model that exhibits computational simplicity and encompasses Rayleigh, pre-Rayleigh, and post-Rayleigh statistics. The Nakagami shape parameter,  $m$ , has been shown sensitive to the number density of scatterers, the different scattering cross-sections, and the presence and absence of periodic structures according to the findings in the computer simulation and phantom studies (Shankar 2000). The feasibility of Nakagami distribution for tissue characterization has been evaluated in benign and malignant breast tumors (Shankar *et al* 2001, 2002), liver fibrosis (Tsui *et al* 2010a), human vocal fold tissue (Tsui *et al* 2011), vaginal fibrosis (Liu *et al* 2012, Yang *et al* 2013), and thermal lesions induced by high intensity focused ultrasound (HIFU) (Li *et al* 2010, Rangraz *et al* 2014).

Despite the promising results of tissue characterization using the shape parameter,  $m$ , of the Nakagami distribution, the reported  $m$  values varied across studies. Tsui *et al* (2008) reported the  $m$  parameter of benign breast masses ( $n = 4$ ) to be  $0.67 \pm 0.11$ , and in a later study, the  $m$  parameter of benign ( $n = 50$ ) and malignant ( $n = 50$ ) lesions being  $0.69 \pm 0.12$  and  $0.55 \pm 0.12$ , respectively (Tsui *et al* 2010b). In the same year and in a smaller cohort of patients, Tsui *et al* published the  $m$  values of benign ( $n = 30$ ) and malignant ( $n = 30$ ) breast masses to be 0.7 and 0.58, respectively (Tsui *et al* 2010b). Good agreement in  $m$  values for benign and malignant breast tumors was shown among these studies. However, Liao *et al* showed that the benign ( $n = 25$ ) and malignant ( $n = 25$ ) breast tumors had  $m$  values of  $0.59 \pm 0.13$  and  $0.50 \pm 0.12$ , respectively (Liao *et al* 2012), both of which were much lower than those in Tsui's reports. Moreover, in the aforementioned studies, Nakagami imaging was only applied to the focal zone, which might be related to the lack of uniformity in a larger imaging zone in their Nakagami imaging paradigm, while clinical imaging favors a large field of view for diagnosis.

Since the statistics of the backscattered envelope are mainly determined by the density and arrangement of scatterers in a resolution cell, several factors influencing the resolution cell may impact the estimation of the statistical parameter, such as the Nakagami  $m$  parameter. In general, variations in the size of the resolution cell are attributed to two groups of factors. One is related to the tissue properties, such as tissue attenuation (Zagzebski *et al* 1999). The intervening tissue attenuation preferentially removes the high frequency component of the ultrasound beam, thus equivalently enlarging the resolution cell and shifting the backscattered envelope statistics into the Rayleigh regime regardless of the actual scatterer density in tissues (Zagzebski *et al* 1999). The other is relevant to the system properties (Tsui and Wang 2004, Tsui and Tsai 2015). As implied in Chen *et al* (1994a), the estimation of statistical parameters varied greatly with different transducer frequencies. The size of the resolution cell also depends on the beamforming methods. For instance, in previous studies, using a focused single element transducer was more sensitive than an unfocused one for low concentration scatterer characterization (Tsui and Wang 2004), and multi-focal beamforming improved the sensitivity in characterizing tissues with low scatterer densities (Tsui and Tsai 2015).

It has been demonstrated that beamforming has a significant effect on the size of the resolution cell and eventually on the statistical parameter estimation. Beamforming methods

providing uniform resolution cells along the depth direction may presumably remedy the issue of  $m$  estimation variations in Nakagami imaging. Nonetheless, to our best knowledge, a systematic study of various beamforming methods for parametric imaging has not been consolidated. Therefore, we attempt to investigate the effects of both conventional and state-of-the-art beamforming methods on Nakagami imaging at different imaging depths. Suggestions on choices of beamforming methods for tissue characterization using Nakagami imaging are also discussed.

## Materials and methods

### *Nakagami distribution*

The probability density function of the envelope of the backscattered radio-frequency (RF) signal (termed as signal in the following text for abbreviation) from tissues,  $f(R)$ , is described by the Nakagami statistical model (Shankar 2000) as follows:

$$f(R) = \frac{2m^m R^{2m-1}}{\Gamma(m)\Omega^m} \exp\left(-\frac{m}{\Omega}R^2\right)U(R), \quad (1)$$

where  $\Gamma(\cdot)$  and  $U(\cdot)$  are the gamma function and unit step function, respectively;  $R$  is the amplitude of the backscattered envelope. In our measurements,  $R$  is obtained by performing the Hilbert transformation to the RF signals. The Nakagami shape parameter ( $m$ ) and the scaling parameter ( $\Omega$ ) are obtained from the following equations (Shankar 2000)

$$m = \frac{[E(R^2)]^2}{E[R^2 - E(R^2)]^2}, \quad (2)$$

$$\Omega = E(R^2). \quad (3)$$

where  $E(\cdot)$  denotes the statistical mean. The Nakagami parameter  $m$  is estimated in this study to describe the statistics of the envelope of the backscattered signal. The statistics of the backscattered envelope follows the Rayleigh distribution when  $m$  equals 1. When  $m$  is smaller or larger than 1, the envelope statistics conform to a pre-Rayleigh or a post-Rayleigh distribution, respectively (Shankar 2000).

### *Beamforming methods*

A programmable ultrasound system (Vantage 256, Verasonics, Redmond, WA, USA) equipped with a linear array probe (L7-4; 128 elements; Advanced Technology Laboratories, Bothell, WA, USA) operating at 5 MHz was used to realize various beamforming methods. Ultrasound radio-frequency (RF) signals were sampled at 20 MHz, and in-phase and quadrature (IQ) data were acquired.

Single-focusing (SF), multi-focusing (MF), synthetic aperture (SA) (Jensen *et al* 2006) and coherent plane wave compounding (CPWC) (Montaldo *et al* 2009) were implemented and evaluated in this study. The best resolution for SF reconstructed images was intrinsically achieved within the focal zone, while expanded resolution cells were found outside the focal zone. The MF method has previously been applied in Nakagami imaging (Tsui and Tsai 2015). In our study, the number of foci for an optimal MF was determined by dividing the entire imaging depth by the  $-6$  dB length of the focal zone (13.0 mm). Dynamic receive focusing was applied in both

of the SF and MF methods. Meanwhile, SA (Jensen *et al* 2006) and CPWC (Montaldo *et al* 2009) methods have emerged in ultrasound imaging to provide high quality images in terms of spatial resolution and contrast, as well as a uniform resolution cell throughout the imaging field of view (FOV). In SA, each element in the linear array probe was subsequently used to transmit a cylindrical ultrasound wave and a finite aperture was used to receive the echoes to reconstruct a low resolution, one-way focused image that covered the FOV. Summation of the 128 resultant low resolution images formed a high resolution image with two-way focusing. For CPWC, 64 steered plane waves were emitted sequentially, with an overall angular aperture of  $28.64^\circ$  from  $-14.32^\circ$  to  $14.32^\circ$  at  $0.45^\circ$  increments, and the beamformed data of each plane wave insonification were coherently compounded (Montaldo *et al* 2009). Note that a constant f number ( $F_\# = 2$ ) was used both in transmission and reception for the MF, SA, and CPWC methods, and a constant f number ( $F_\# = 2$ ) in reception was employed for the SF method.

### Resolution tests

The axial and lateral spatial resolutions are conventionally measured from the widths of the point spread functions (PSFs) of the ultrasound imaging system, using a small point target in a homogeneous medium (Shung 2005). For instance, a line or a wire target inside a quality assurance phantom can be employed (Papp 2011). In our study, the wire targets in a commercial, tissue-mimicking calibration phantom (Model 040GSE, CIRS, Norfolk, VA, USA) were utilized to measure the axial and lateral resolutions in different beamforming regimes. The wire targets were made of nylon monofilaments and measured at  $100\ \mu\text{m}$  in diameter according to the manufacturer. The five targets studied were located from 1 to 5 cm at 1 cm increments (figure 1). The optimal MF was achieved with five foci to ensure that every target was positioned in the middle of a focal zone, while the transmit focus in the SF method was at the second target. Full width at half maximum (FWHM) of the point spread function (PSF) of each target was calculated as the axial and lateral resolutions (i.e. the size of the resolution cell) at each of the five different imaging depths.

### Ultrasound image simulation

Ultrasound image simulation was carried out by the Field II simulation program (Jensen and Svendsen 1992, Jensen 1996). To simulate the L7-4 probe (Advanced Technology Laboratories, Bothell, WA, USA) used in our phantom experiments (see the following section), a linear array probe with 128 elements and a center frequency of 5 MHz was modeled. The pitch was 0.3 mm and the kerf was 0.05 mm with an aperture size of 45 mm. One cycle of a sine burst of the center frequency of 5 MHz was considered for the transducer excitation. The sampling rate was 100 MHz. Scatterers were randomly placed from 1.5 to 60 mm with a lateral width of 80 mm. The amplitudes of scatterers followed the normal distribution. Six different scatterer densities were modeled, including 2, 4, 8, 16, 32, and 64 scatterers  $\text{mm}^{-3}$ . The speed of sound was assumed to be  $1540\ \text{m s}^{-1}$ . Please note that the simulations did not model the frequency dependence of scattering since point scatterers were used.

For the SF method, a transmission focus was placed at the imaging depth of 23 mm, and the focal zone was 13 mm in length. The MF method was achieved by placing four foci at 10, 23, 36, and 49 mm. In transmission, the CPWC method was performed with 64 plane waves with steering angles ranging from  $-14.32^\circ$  to  $14.32^\circ$  at  $0.45^\circ$  increments. A single element transmission with a total of 128 transmissions was adopted in the SA method. In reception of the SF, MF, and CPWC methods, dynamic focus beamforming was used. A constant f number



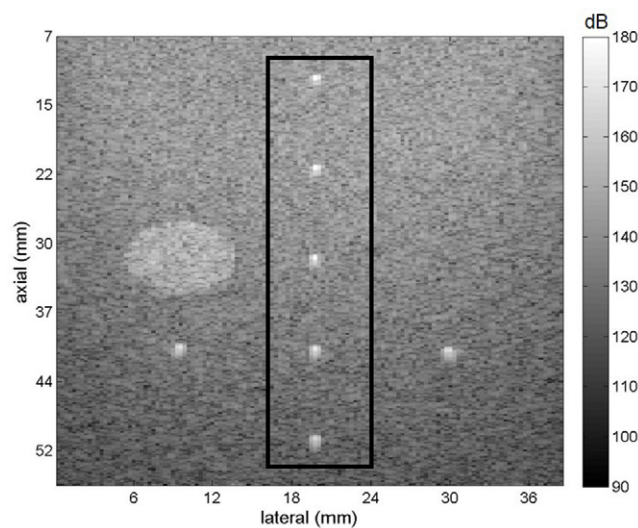


**Figure 1.** A B-mode image of a commercial calibration phantom reconstructed based on the synthetic aperture (SA) method with wire targets used for the resolution test.

( $F_{\#} = 2$ ) was used both in transmission and reception for CPWC, SA, and MF, and in reception for the SF method. The spatial (axial  $\times$  lateral) resolutions estimated and averaged along the depth in CPW, SA, SF, and MF simulations were  $0.31 \text{ mm} \times 0.48 \text{ mm}$ ,  $0.32 \text{ mm} \times 0.31 \text{ mm}$ ,  $0.32 \text{ mm} \times 0.61 \text{ mm}$ , and  $0.31 \text{ mm} \times 0.56 \text{ mm}$ , respectively.

#### Homogenous phantom

To ensure a large homogeneous region for analysis, experiments were performed on home-made homogeneous gelatin–agar phantoms to test the beamforming effects. Based on a recipe in a previous study (Madsen *et al* 2005), soft-tissue mimicking phantoms were prepared by dissolving 5.5% gelatin (Sigma-Aldrich, St. Louis, MO, USA) and 3.0% agar (Sigma-Aldrich, St. Louis, MO, USA) in de-ionized water. The scattering was contributed from the spherical glass beads (Supelco, 59200U, Bellefonte, PA, USA) with an average diameter of  $75 \pm 5 \mu\text{m}$  and a density ( $\rho$ ) of  $3000 \text{ kg m}^{-3}$  (Kruglenko *et al* 2013). Neglecting the small variation in the diameter of glass beads, the concentration,  $C$ , of the scatterers in each gelatin–agar phantom could be calculated using the following equation:

$$C = \frac{M}{\frac{4}{3}\pi r^3 \cdot \rho \cdot V}, \quad (4)$$

where  $M$  and  $r$  represent the mass and the radius of the glass beads, respectively, and  $V$  denotes the volume of the gelatin–agar solution. We prepared phantoms with three different scatterer concentrations of 16, 32, and 64 scatterers  $\text{mm}^{-3}$ . The gelatin–agar solution (250 ml) with glass beads was then continuously stirred by a magnetic stirrer until it congealed to reach a random distribution of scatterers in the solution and to prevent scatterers from sedimentation. The speed of sound and acoustic attenuation of the three phantoms with different scatterer densities were characterized by the through-transmission method (Madsen *et al* 1999).

Beamformed data were yielded using the aforementioned four beamforming methods. Specifically, in the SF scenario, the focus was at 21.9 mm. A total of four foci at 8.9, 21.9,

34.9, and 47.9 mm were selected in the optimal MF to cover the entire imaging depth of 55.3 mm. Five repeated acquisitions were performed for each beamforming method.

#### *Nakagami parametric map*

A Nakagami parametric map was yielded from the backscattered envelopes of each homogeneous phantom using a sliding window based method, which is a typical strategy to form ultrasonic parametric maps and has been adopted in previous tissue characterization studies (Tsui and Chang 2007, Tsui *et al* 2010a 2011, Liu *et al* 2012, Yang *et al* 2013, Larrue and Noble 2014). A sliding window, which was a sub-region in an envelope image, was selected to collect the local backscattered envelope data for the estimation of a local Nakagami parameter  $m_{\text{local}}$ . The calculated  $m_{\text{local}}$  was assigned to the sample point located at the center of the sliding window in the corresponding Nakagami parametric map. The 2D Nakagami parametric map was then generated by shifting the sliding window by one signal sample at a time throughout the ultrasound envelope data.

Previous studies (Tsui and Chang 2007, Larrue and Noble 2011) have demonstrated that the size of the sliding window is crucial in the estimation of Nakagami parameters. Decreasing the window size improves the resolution of the Nakagami image while degrading the stability of estimation. Therefore, before constructing a Nakagami parametric map, the size of the sliding window should be determined to balance the trade-off between estimation stability and parametric image resolution. Considering that the envelope statistics of backscattered signals depended on the scatterer distribution in a resolution cell, instead of a conventional square window (Tsui and Chang 2007), the size of the sliding window was chosen to be an integer multiple ( $N$ ) of the size of the resolution cell (Li *et al* 2010) in this study. Specifically, the axial and lateral window lengths were equal to the same integer multiple ( $\sqrt{N}$ ) of the axial and lateral resolutions, respectively. We took the average measurements from the first, second, third, and fifth string targets in the calibration phantom as the resolution sizes for each beamforming method. Note that the string target locations in the calibration phantom matched the centers of the four focal zones in our home-made homogeneous phantoms. Both the SA and CPWC beamformed data were utilized to determine the optimal integer multiple ( $N$ ), because they, in theory, achieved constant axial and lateral resolutions throughout the FOV. A total of seven window sizes were evaluated in our study. Parametric maps were generated with  $\sqrt{N}$  varying from 1 to 7. The mean and the standard deviation of  $m$  values within an FOV of 50.9 mm  $\times$  12.0 mm on the parametric map were compared for different values of  $\sqrt{N}$ . The smallest  $\sqrt{N}$  that rendered the mean and the standard deviation of  $m$  values close to a steady estimation was selected in our study.

Using the window size with the selected  $\sqrt{N}$ , the performance of the beamforming-specific window was evaluated as follows. Two different types of windows were used to generate parametric maps from the same beamformed data. First, the same window size was applied for all four beamforming methods. We chose  $N$  times the SA's resolution as the window, since it exhibited the best spatial resolution according to our resolution test. This was termed as a beamforming-invariant method. Second, a window was chosen as  $N$  times the spatial resolution of each beamforming method. Therefore, actual window sizes varied with beamforming methods but contained exactly the same number of resolution cells. This was termed as a beamforming-specific method. The responses of Nakagami  $m$  parameters to different scatterer densities were additionally studied using the beamforming-specific method. Within the 50.9 mm  $\times$  12 mm FOV on a Nakagami parametric map, the mean  $m$  values were compared among phantoms with different scatterer densities for each beamforming method.



In order to further illustrate the depth-dependency of Nakagami imaging, a region of interest (ROI) of 11.8 mm  $\times$  12.0 mm was used to collect the estimated  $m$  parameters. The shifting ROIs covered the imaging depths from 11 to 52 mm at a step size of 1 mm in the axial direction. The distribution of estimated  $m$  parameters within each ROI was characterized by its mean, variance, and skewness. Skewness or the third moment is a measure of the asymmetry of the distribution. For a unimodal distribution, a positive value means the mass of the distribution is concentrated on the left side of the distribution, whereas a negative value exhibits the mass of the distribution concentrated on the right side of the distribution. A zero skew indicates a symmetrical distribution. The mean, variance, and skewness of five repeated measurements were expressed as their own mean  $\pm$  standard deviation (SD). Note that for the following statistical analyses, four ROIs of 11.8 mm  $\times$  12.0 mm inside the FOV were typically identified, matching the four focal zones of MF. Statistical analyses on the mean, variance, and skewness within these four zones for all beamforming methods were performed.

Note that as the lateral resolution of SF was expected to have a relatively large variation to the imaging depth, we also evaluated the performance of the beamforming-specific, depth-dependent window for SF beamformed data. In this case, the  $m$  values in each ROI were calculated based on a window containing  $N$  times the resolution at its corresponding depth (see table 1). The statistics of the  $m$  distribution were compared with the results obtained using the beamforming-specific but depth-invariant window.

#### *Statistical analysis*

Statistical analyses were performed in Matlab (The Mathworks, Natick, MA, USA). Effects of beamforming and its depth dependency were assessed by the two-way ANOVA for the beamforming-invariant and beamforming-specific parametric maps at four zones mentioned in the previous section. Depth dependency for each beamforming method was, on the other hand, assessed by one-way ANOVA tests. Power analysis (alpha level ( $\alpha$ ) = 0.001) was performed to assure an adequate power to detect the statistical significance. Responses of the Nakagami  $m$  parameter to different scatterer densities were additionally assessed by the one-way ANOVA tests. Post hoc analyses were performed using the Bonferroni procedure for pairwise comparisons. Significance was assumed if  $p < 0.001$ .

## **Results**

#### *Resolution test*

The axial and lateral resolutions as a function of the imaging depth measured from the calibration phantom are shown in figure 2. The axial resolutions were relatively uniform at different imaging depths in all beamforming methods. The lateral resolutions were generally poorer than the axial ones and varied with the imaging depth in the SF case. In contrast, lateral resolutions of CPWC, SA, and MF were less dependent on the imaging depth as expected; the lateral resolution of SA was found to be the finest. The measured spatial resolutions in all studied beamforming methods are listed in table 1.

#### *Phantom characteristics*

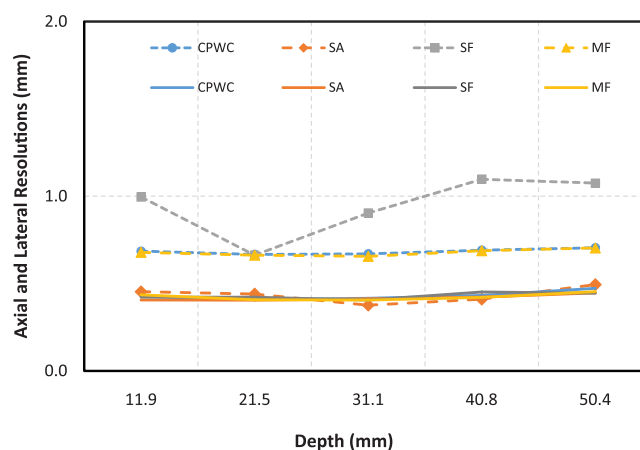
The measured speed of sound in de-gassed water at 23 °C was  $1501 \pm 11$  m s<sup>-1</sup> (table 2). With the same experimental setting, the speeds of sound in gelatin–agar phantoms with

**Table 1.** Beamforming methods and their corresponding imaging resolutions.

Beamforming	Resolution cell (mm <sup>2</sup> )
	Axial $\times$ Lateral
SA	0.42 $\times$ 0.43
CPWC	0.43 $\times$ 0.68
MF	0.42 $\times$ 0.68
SF <sup>a</sup>	0.43 $\times$ 0.95
<i>Depth-dependent<sup>b</sup></i>	
Zone 1	0.44 $\times$ 0.68
Zone 2	0.41 $\times$ 0.66
Zone 3	0.41 $\times$ 0.66
Zone 4	0.45 $\times$ 0.70

<sup>a</sup> Averaged axial and lateral resolutions when SF was focused at zone 2.

<sup>b</sup> Resolutions for SF depth-dependent method at zone 1–4 corresponded to the resolutions of the 1st, 2nd, 3rd, and 5th wire targets in the calibration phantom.

**Figure 2.** Axial (solid lines) and lateral (dashed lines) resolutions of CPWC, SA, SF, and MF measured from the wire targets in a commercial calibration phantom.**Table 2.** Characteristics of the gelatin–agar phantoms.

Scatterer density (mm <sup>-3</sup> )	Speed of sound in water (m s <sup>-1</sup> )	Speed of sound in phantom (m s <sup>-1</sup> )	Attenuation coefficient at 5 MHz (dB cm <sup>-1</sup> )
16	1501 $\pm$ 11	1520 $\pm$ 5	0.22 $\pm$ 0.02
32		1530 $\pm$ 1	0.26 $\pm$ 0.01
64		1525 $\pm$ 3	0.66 $\pm$ 0.00

scatterer densities of 16, 32, and 64 scatterers mm<sup>-3</sup> were 1520  $\pm$  5 m s<sup>-1</sup>, 1530  $\pm$  1 m s<sup>-1</sup>, and 1525  $\pm$  3 m s<sup>-1</sup>, respectively. These were comparable to the speed of sound measured in a previous study (Madsen *et al* 2005) (1532–1542 m s<sup>-1</sup> at 22 °C in gelatin–agar phantoms). The attenuation coefficients in our home-made phantoms with scatterer densities of 16 scatterers mm<sup>-3</sup>, 32 scatterers mm<sup>-3</sup>, and 64 scatterers mm<sup>-3</sup> were found to be 0.22  $\pm$  0.02 dB cm<sup>-1</sup>, 0.26  $\pm$  0.01 dB cm<sup>-1</sup>, and 0.66  $\pm$  0.00 dB cm<sup>-1</sup> at 5 MHz, respectively. These were weak compared to that in real soft tissues, for instance, 1.30–1.61 dB cm<sup>-1</sup> at 1 MHz in

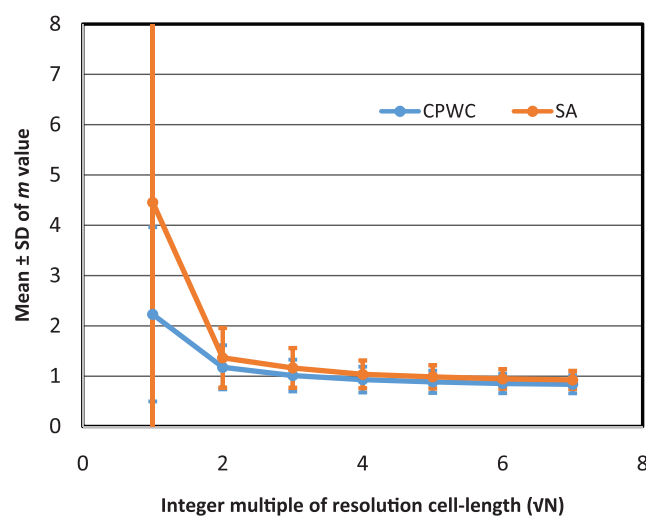


**Figure 3.** Mean and standard deviation of  $m$  values estimated using different integer multiples ( $\sqrt{N}$ ) of the resolution cell lengths based on SA and CPWC beamformed data of the home-made homogeneous phantom with the scatterer density of 64 scatterers  $\text{mm}^{-3}$ .

muscle (Christensen 1988). Therefore, the attenuation effects in our home-made phantoms were neglected.

Figure 3 shows the mean  $m$  values within the 50.9 mm  $\times$  12.0 mm FOV of the homogeneous phantom as a function of  $\sqrt{N}$ . The mean  $m$  values decreased with increasing  $\sqrt{N}$ ; the variation of  $m$  values within the FOV depicted by the standard deviation decreased with increasing  $\sqrt{N}$ . To balance the trade-off between estimation stability and Nakagami image resolution, four-fold ( $\sqrt{N} = 4$ ) the axial and lateral resolutions were chosen as the sliding window lengths.

### Simulation results

Figures 4 and 5 shows the simulation results obtained with CPWC, SA, SF, and MF beamforming with scatterer density ranging from 2 to 64 scatterer  $\text{mm}^{-3}$ . Beamforming-specific windows were used. Figure 4 shows that the mean Nakagami  $m$  parameter within the FOV increased with the scatterer density in the four beamforming cases studied. Figure 5 shows that the mean  $m$  values obtained from CPWC, SA, and MF beamforming methods were relatively depth-invariant compared with those yielded from the SF method. Specifically, the  $m$  values obtained from the SF method were the lowest and agreed quantitatively with the  $m$  estimates from other methods at the vicinity of 25 mm, where the focal zone in SF was.

Figure 6 demonstrates the response of Nakagami  $m$  parameters to various scatterer densities. The  $m$  parameters for the phantom with 16 scatterers  $\text{mm}^{-3}$  were significantly smaller than those from phantoms with 32 and 64 scatterers  $\text{mm}^{-3}$  ( $p < 0.001$ ), regardless of beamforming methods. No significant differences were found between the  $m$  parameters from phantoms with 32 and 64 scatterers  $\text{mm}^{-3}$  ( $p = 0.0514, 0.0962, 0.7475$ , and  $0.0691$  for CPWC, SA, SF, and MF, respectively).

Figure 7 shows the beamforming effects on  $m$  value estimation as a function of depth in the home-made homogeneous phantom whose scatterer density was 64 scatterers  $\text{mm}^{-3}$ . Calculation with beamforming-specific window sizes (figures 7(a)–(c)) has the following two

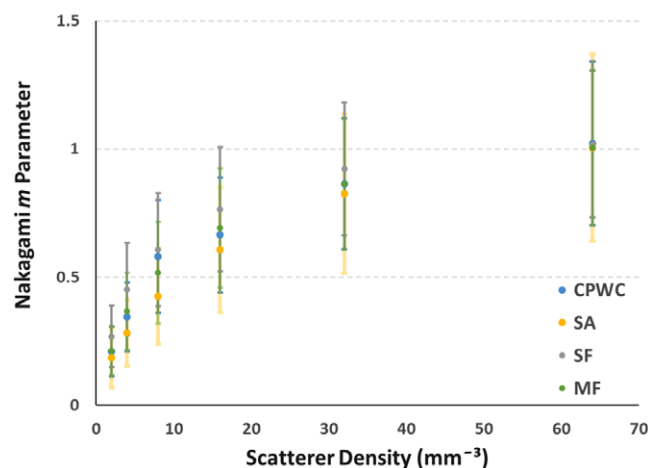


**Figure 4.** The estimated Nakagami  $m$  parameter (mean  $\pm$  standard deviation) as a function of scatterer densities in simulated homogeneous phantoms in CPWC (blue), SA (orange), SF (gray), and MF (green) beamforming methods. Beamforming-specific windows were used.

advantages over the beamforming-invariant window sizes (figures 7(d)–(f)), especially for SF beamformed signals. First of all, the overestimating effect appearing at 23–49 mm using the SF method was suppressed. Moreover, variance of  $m$  values within the shifting ROI at 23–49 mm was reduced when using a beamforming-specific window for parametric imaging. On the other hand, the profile of  $m$  values estimated from CPWC, SA, or MF beamformed data as a function of imaging depth was less dependent on the window size. Skewness of  $m$  values generally fluctuated with imaging depths for all beamforming methods, especially for SF beamformed signals using the beamforming-invariant window size, showing more positively skewed at 23–49 mm.

Statistical analyses on the mean  $m$  values within the four zones in the home-made homogeneous phantom whose scatterer density was 64 scatterers  $\text{mm}^{-3}$  revealed that beamforming had a significant impact on  $m$  value estimation. Shown in figure 2 and table 3, when using a beamforming-invariant window,  $m$  values from SF beamformed signals were significantly different from those using CPWC and SA ( $p < 0.005$ ). In contrast, as listed in table 4,  $m$  values calculated from SF beamformed signals using the beamforming-specific window were comparable to those using CPWC and MF. Meanwhile,  $m$  values from CPWC beamformed signals were the lowest ( $p < 0.001$ ) and close to unity, while  $m$  values from SA were found statistically different from those from other beamforming methods using beamforming-specific windows ( $p < 0.001$ ). Furthermore, for SF beamformed signals, the  $m$  values with the depth-dependent window were not statistically different from those with beamforming-specific SF ( $p = 0.1628$ ), MF ( $p = 0.8051$ ), and CPWC ( $p = 0.2055$ ). The powers for the two-way ANOVA tests were 100%.

The post hoc analyses show that mean  $m$  values from MF signals were not depth-dependent regardless of windows used ( $p < 0.001$ ). Those from CPWC signals were not depth-dependent when using the beamforming-specific windows ( $p < 0.001$ ), either. Mean  $m$  values from SA signals at the deepest zone were higher than those in the other three zones although the difference in  $m$  values was within a small range (0.04–0.10). In table 5, mean  $m$  values from SF signals in the bottom two zones were significantly higher than the upper two zones ( $p < 0.001$ ) with a difference of 0.05–0.07. This variation relevant

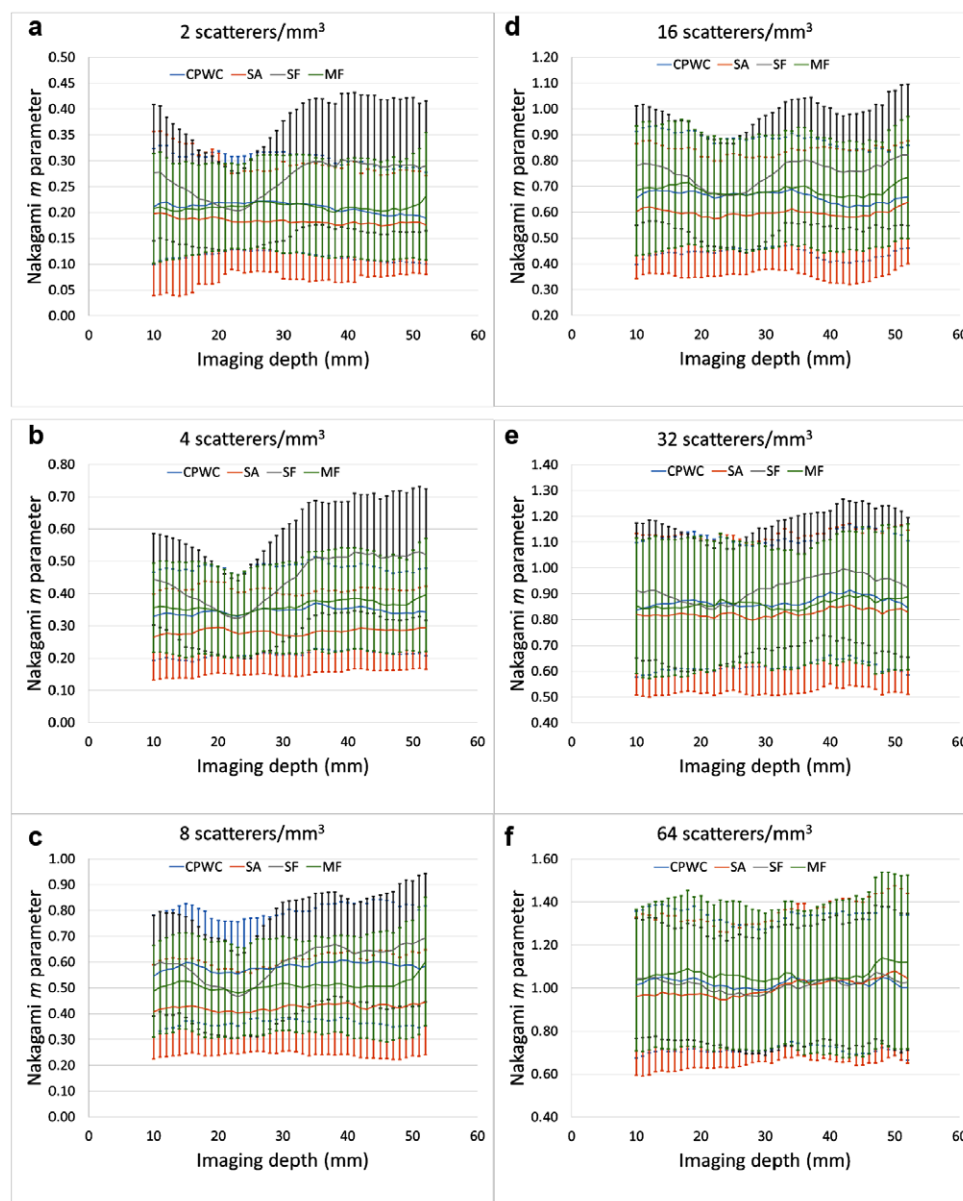


**Figure 5.** The estimated Nakagami  $m$  parameter (mean  $\pm$  standard deviation) as a function of the imaging depth in simulated homogeneous phantoms with scatterer densities of 2, 4, 8, 16, 32, and 64 scatterers mm<sup>-3</sup> (a)–(f). Beamforming-specific windows were used.

to imaging depths was reduced by applying the depth-dependent window for SF beamformed signals. The differences between the two top and two bottom zones were reduced to 0.01–0.05.

Statistical analyses on the variance of  $m$  values within the four zones also demonstrated significant dependence on beamforming. Although the variances were generally low around

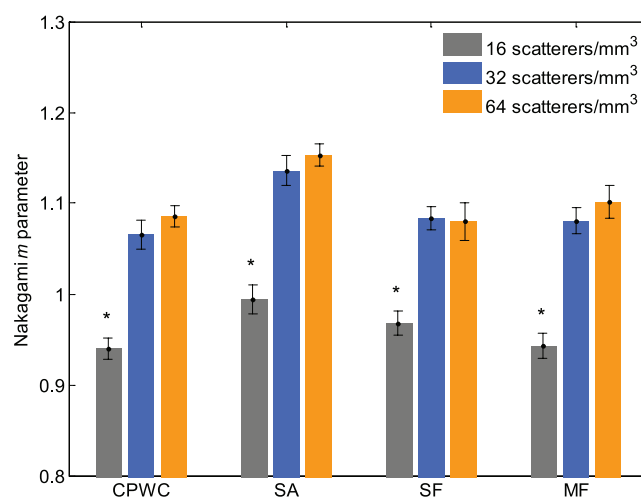


**Figure 6.** Nakagami  $m$  parameters estimated from CPWC, SA, MF, and SF beamformed data of homogeneous gelatin–agar phantoms with different scatterer densities. (\*The mean Nakagami  $m$  parameter within the  $50.9\text{ mm} \times 12\text{ mm}$  FOV of five repeated measurements for the indicated scatterer density was significantly different from that of all the other scatterer densities. Significance level is 0.001.)

0.1, when using a beamforming-invariant window, variances of  $m$  values from SF signals were significantly higher than the other forms of signals ( $p < 0.001$ ). Applying the beamforming-specific window, variances of  $m$  values from SF and CPWC signals became significantly lower than those from SA and MF ( $p < 0.001$ ). Variances in the bottom zone were higher than the top three zones in CPWC, SA and MF, regardless of windows used ( $p < 0.001$ ). Using the beamforming-specific window reduced the high variance at the third zone of SF signals. In contrast, no significant influence of beamforming was found on skewness of  $m$  values throughout the FOV.

## Discussion

The beamforming effects on Nakagami imaging were assessed in our study. The shape parameter,  $m$ , in Nakagami imaging is a quantitative marker associated with scatterer density and their arrangement patterns in space. Previous studies (Chen *et al* 1994a, Zagzebski *et al* 1999, Tsui and Wang 2004, Tsui and Tsai 2015) demonstrated that both tissue properties and transducer parameters influenced Nakagami  $m$  parameter estimation. Due to the beam divergence along the insonification path, lateral resolution deteriorated, leading to unreliable parameter estimation for a large FOV. Therefore, beamforming methods providing a uniform resolution in the FOV (CPWC, SA, and MF) were investigated in our study, and their performances were compared with conventional beamforming methods, such as SF.

As discussed in previous studies (Tsui and Chang 2007, Larrue and Noble 2011), the selection of the sliding window size was crucial for  $m$  parameter estimation, since a smaller window size resulted in better parametric map resolution, while sacrificing the estimation reliability. Therefore, window lengths ranging from 0.86 to 2.70 mm were utilized in  $m$  parameter calculation (Tsui and Chang 2007, Larrue and Noble 2011). However, since the statistics of the backscattered envelope were demonstrated to be associated with the scatterer density and arrangements in one resolution cell (Tuthill *et al* 1988, Shankar 2000), we used window sizes



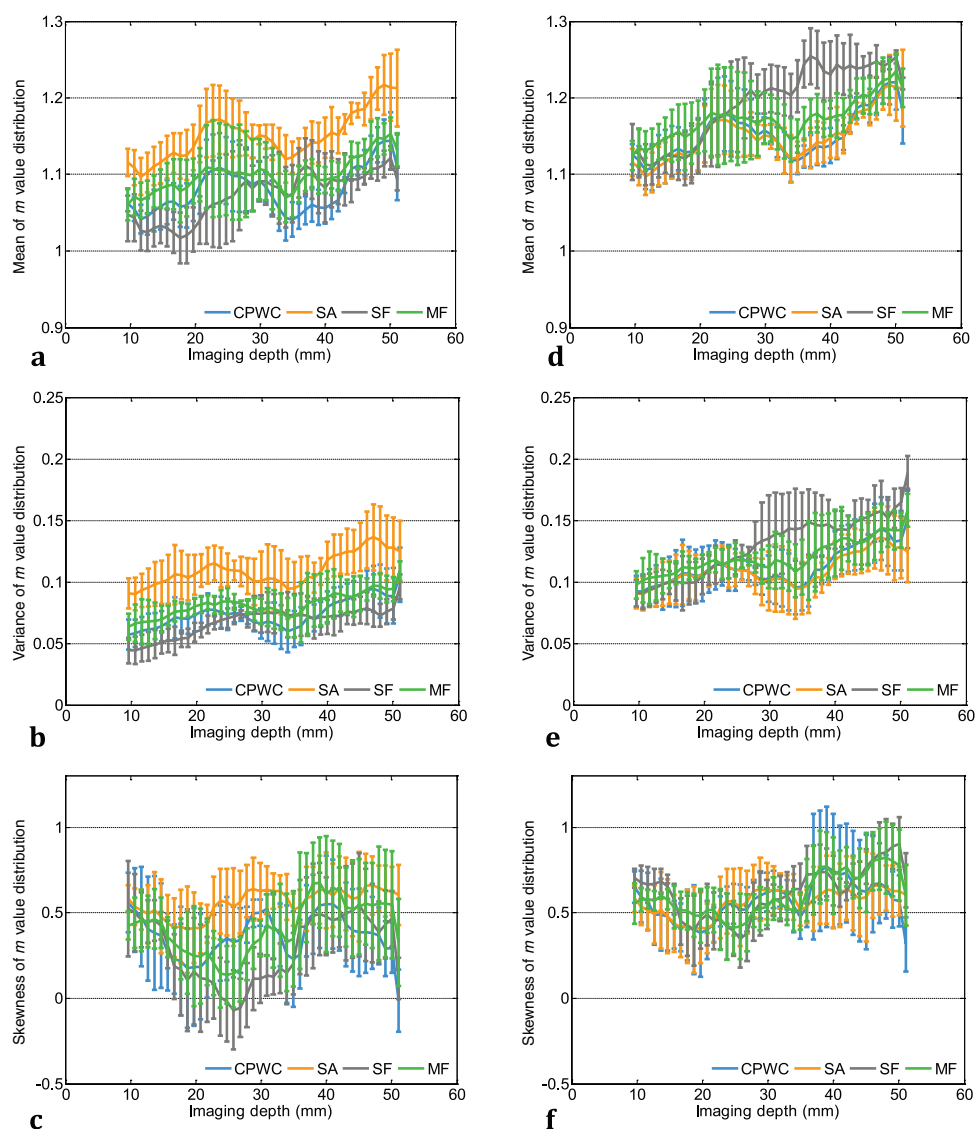


**Figure 7.** Beamforming effects on Nakagami  $m$  value estimation along the imaging depths characterized by its mean (a), (d), variance (b), (e), and skewness (c), (f) using both beamforming-specific (a)–(c) and beamforming-independent window sizes (d)–(f) on all forms of beamformed data of the home-made homogeneous gelatin–agar phantom with the scatterer density of 64 scatterers  $\text{mm}^{-3}$ .

that were integer multiples of the resolution cell to ensure the same number of resolution cells within each window. Tested on the SA and CPWC beamformed signals of the home-made gelatin–agar phantom with the scatter density of 64 scatterers  $\text{mm}^{-3}$ , a window containing 16 resolution cells ( $\sqrt{N} = 4$ ) provided the best balance between stable estimation and fine parametric map resolution as shown in figure 3.

The estimated Nakagami  $m$  parameter as a function of scatterer density in homogeneous phantoms was first confirmed both *in silico* and *in vitro*. Shown in figures 4 and 6,

**Table 3.** Differences of mean  $m$  values obtained by beamforming-invariant windows in the home-made homogeneous phantom whose scatterer density was 64 scatterers  $\text{mm}^{-3}$  (I–J,  $n = 5$ ).

	CPWC (I)	SA (I)	MF (I)
SF (J)	−0.04 <sup>a</sup>	−0.05 <sup>a</sup>	−0.02
MF (J)	−0.02	−0.02	
SA (J)	0.00		

<sup>a</sup>  $p < 0.005$ .**Table 4.** Differences of mean  $m$  values obtained by beamforming-specific windows in the home-made homogeneous phantom whose scatterer density was 64 scatterers  $\text{mm}^{-3}$  (I–J,  $n = 5$ ).

	CPWC (I)	SA (I)	MF (I)	SF (I)
SF (J) <sup>a</sup>	−0.01	0.05 <sup>b</sup>	0.00	0.00
SF (J)	0.01	0.07 <sup>b</sup>	0.02	
MF (J)	−0.02	0.05 <sup>b</sup>		
SA (J)	−0.07 <sup>b</sup>			

<sup>a</sup> Depth-dependent, beamforming-specific windows applied on SF beamformed data.<sup>b</sup>  $p < 0.001$ .**Table 5.** Depth-dependency of mean  $m$  values from SF beamformed method (I–J,  $n = 5$ ).

Depth-independent window	Zone 4 (I)	Zone 3 (I)	Zone 2 (I)
Zone 1 (J)	0.07 <sup>a</sup>	0.07	0.02
Zone 2 (J)	0.06	0.05	
Zone 3 (J)	0.01		
Depth-dependent window	Zone 4 (I)	Zone 3 (I)	Zone 2 (I)
Zone 1 (J)	0.05	0.03	0.05
Zone 2 (J)	0.01	0.02	
Zone 3 (J)	0.02		

<sup>a</sup>  $p < 0.001$ .

the observation that  $m$  values generally declined with decreasing scatterer density within a resolution cell was in good agreement with literature (Shankar 2000, Tsui and Chang 2007), regardless of the beamforming paradigms. In the home-made phantoms with scatterer density of 32 and 64 scatterers  $\text{mm}^{-3}$ , the envelope statistics approached the Rayleigh distribution, and the  $m$  values were close to 1 as there were more than 10 scatterers in a resolution cell. When the scatterer density was below 16 scatterers  $\text{mm}^{-3}$ , the envelope statistics became pre-Rayleigh, and the  $m$  values were found to be significantly different from those estimated from phantoms with higher scatterer densities (figure 6).

In this study, a beamforming-specific window strategy was proposed for the fair comparison of the depth dependency among beamforming methods. Related to the variance (second moment) of the envelope within the window, the  $m$  parameter estimated from equation (2) could be affected by the number of speckles (resolution cells) in the window. Fewer speckles led to smaller variances, thus overestimating  $m$  values. In the simulation, overestimation of the  $m$

values from SF beamformed data with the beamforming-specific window was observed outside the SF focal zone, exhibiting the depth-variant  $m$  estimation owing to the depth-varying lateral resolutions in SF (figure 5). Such depth-variance of  $m$  estimation was not prominent in the simulated phantom with 64 scatterers  $\text{mm}^{-3}$  (figure 5(f)) possibly because of both the sufficient number of scatterers present in a resolution cell and the relatively small variations of lateral resolutions. In the home-made phantom with 64 scatterers  $\text{mm}^{-3}$ , overestimation of the  $m$  values was manifested in SF beamformed signals using the beamforming-independent window (figure 7(d)). When  $m$  parameters from SF signals were estimated using the beamforming-specific window size, the overestimated  $m$  values outside the focal zone, especially at 26–49 mm, were greatly reduced. The  $m$  parameter estimation using beamforming-specific windows was proven to be less dependent on the beamforming methods. In addition, CPWC, SA, and MF with beamforming-specific windows were less dependent on imaging depth windows. This observation was in good accordance with the relatively uniform lateral resolutions at different imaging depths. SF, on the other hand, exhibited a large variation in the lateral resolution (figure 2) along the imaging depth, so beamforming-specific depth-dependent windows were required to reduce the differences in  $m$  estimates between the far and near imaging zones (table 5).

Table 4 and figure 6 show statistically higher ( $p < 0.001$ )  $m$  estimates from SA than from other methods, all using beamforming-specific windows, in the phantom study. A similar finding was also observed from the kernel test shown in figure 3. This might have stemmed from the slightly depth-variant lateral resolution (figure 2), which was also found comparable to the axial resolution in SA (table 1). The average effective window kernel size in SA was therefore much smaller than that in other methods, leading to  $m$  estimates deviating from those obtained in CPWC and MF. Despite the relatively high  $m$  values from SA beamformed data,  $m$  estimates obtained using the beamforming-specific window were found to be depth-independent as demonstrated in table 4 and the post hoc analysis.

Our findings suggest that  $m$  parameter estimation based on the SF beamforming method was depth-variant when beamforming-invariant windows were utilized. This may hinder its application for tissue characterization in clinical practice. Since SF was typically adopted and implemented in previous Nakagami imaging studies, locations of target tissues should be taken into account for the  $m$  value interpretation. Although beamforming-specific depth-dependent windows used for SF beamformed data were found to reduce the variation of  $m$  values at different depths, it would generate a parametric map with non-uniform resolution.

To overcome the effects of beamforming methods on Nakagami imaging, SA, MF, and CPWC are recommended. SA is capable of providing uniform two-way focusing throughout the FOV, while optimal MF allows coverage of the entire image with multiple focal zones. The frame rate of MF is limited by the imaging depth and the number of scan lines for constructing an image. SA can achieve a higher frame rate by recursive imaging although the image resolution is abated (Jensen *et al* 2006). CPWC can also theoretically provide uniform focusing for the entire image and achieve very high frame rates without significantly degrading the image quality by altering the number of plane wave emissions (Montaldo *et al* 2009). In our separate study, we have, for the first time, reconstructed Nakagami  $m$  parametric maps from CPWC-based ultrasound signals of the porcine myocardium *in vitro*. Our findings have shown that  $m$  distributions in the middle layers were statistically different from those in the subepicardial and subendocardial layers ( $p < 0.05$ ) (Yu and Lee 2014). Therefore, users may choose from the aforementioned three beamforming methods according to the clinical applications.

In addition, we found in a separate preliminary study that a heterogeneous layer of pork skeletal muscle (9 mm thick) in front of a homogeneous region of interest in a commercial calibration phantom did not alter the  $m$  values at different imaging depths. Whether other types of tissues whose acoustic parameters are different from the neighboring tissue region

of interest influence  $m$  estimation requires further investigations and is beyond the scope of this study. Other potential parameters may also affect the  $m$  parameter estimation, i.e. the  $f$  number. As the  $f$  number is the ratio of the focal length and the aperture size, smaller  $f$  numbers result in better focusing and thus finer image resolution. Because  $f$  number has a similar mechanism to transducer's frequency and beamforming (Chen *et al* 1994a, Tsui and Wang 2004, Tsui and Tsai 2015) in affecting the  $m$  parameter estimation, its effect was not assessed in our study.

In conclusion, the effects of beamforming methods on Nakagami imaging were investigated in simulations and in the homemade homogeneous phantoms in our study. Our findings show that the size of the resolution cell of SA, MF, and CPWC was relatively independent of imaging depths and thus resulted in comparatively constant  $m$  value estimations. SF, in contrast, exhibited a large variation in resolutions and subsequently in  $m$  parameter estimations along the imaging depth. Therefore, beamforming methods that ensure uniform spatial resolution throughout the imaging FOV is recommended for Nakagami imaging, especially for inter-institutional studies.

## Acknowledgments

This work is partly supported by the Research Grants Council of Hong Kong (ECS 739413E) and the University Development Fund. We would also like to thank Mr Billy Y S Yiu from the Department of Electrical and Electronic Engineering at the University of Hong Kong for his advices on the attenuation measurement of tissue-mimicking phantoms.

## References

- Bercoff J, Tanter M and Fink M 2004 Supersonic shear imaging: a new technique for soft tissue elasticity mapping *IEEE Trans. Ultrason. Ferroelectr. Freq. Control* **51** 396–409
- Burckhardt C B 1978 Speckle in ultrasound B-Mode scans *IEEE Trans. Sonics Ultrason.* **25** 1–6
- Céspedes I, Ophir J, Ponnekanti H and Maklad N 1993 Elastography: elasticity imaging using ultrasound with application to muscle and breast *in vivo Ultrason. Imag.* **15** 73–88
- Chen J F, Zagzebski J A and Madsen E L 1994a Non-Gaussian versus non-Rayleigh statistical properties of ultrasound echo signals *IEEE Trans. Ultrason. Ferroelectr. Freq. Control* **41** 435–40
- Chen J F, Zagzebski J A and Madsen E L 1994b Statistical uncertainty in estimates of an effective scatterer number density for ultrasound *J. Acoust. Soc. Am.* **96** 2556–63
- Christensen D A 1988 *Ultrasonic Bioinstrumentation* (New York: Wiley)
- Destempes F and Cloutier G 2010 A critical review and uniformized representation of statistical distributions modeling the ultrasound echo envelope *Ultrasound Med. Biol.* **36** 1037–51
- Dutt V and Greenleaf J F 1994 Ultrasound echo envelope analysis using a homodyned K-distribution signal model *Ultrason. Imaging* **16** 265–87
- Feleppa E J *et al* 1996 Typing of prostate tissue by ultrasonic spectrum analysis *IEEE Trans. Ultrason. Ferroelectr. Freq. Control* **43** 609–19
- Ho M C, Lin J J, Shu Y C, Chen C N, Chang K J, Chang C C and Tsui P H 2012 Using ultrasound Nakagami imaging to assess liver fibrosis in rats *Ultrasonics* **52** 215–22
- Insana M F, Hall T J and Fishback J L 1991 Identifying acoustic scattering sources in normal renal parenchyma from the anisotropy in acoustic properties *Ultrasound Med. Biol.* **17** 613–26
- Jensen J A 1996 *10th Nordic-Baltic Conference on Biomedical Imaging Published in Medical & Biological Engineering and Computing* vol 34, supplement 1, part 1 pp 351–3
- Jensen J A, Nikolov S I, Gammelmark K L and Pedersen M H 2006 Synthetic aperture ultrasound imaging *Ultrasonics* **44** e5–15
- Jensen J A and Svendsen N B 1992 Calculation of pressure fields from arbitrarily shaped, apodized, and excited ultrasound transducers *IEEE Trans. Ultrason. Ferroelectr. Freq. Control* **39** 262–7
- Konofagou E E, D'hooge J and Ophir J 2002 Myocardial elastography—a feasibility study *in vivo Ultrasound Med. Biol.* **28** 475–82

- Kruglenko E, Gambin B and Cieřlik L 2013 Soft tissue-mimicking materials with various number of scatterers and their acoustical characteristics *Hydroacoustics* **16** 121–8
- Kuc R 1980 Clinical-application of an ultrasound attenuation coefficient estimation technique for liver pathology characterization *IEEE Trans. Biomed. Eng.* **27** 312–9
- Larrue A and Noble J A 2011 Nakagami Imaging with Small Windows 2011 8th IEEE Int. Symp. on Biomedical Imaging: From Nano to Macro pp 887–90
- Larrue A and Noble J A 2014 Modeling of errors in Nakagami imaging: illustration on breast mass characterization *Ultrasound Med. Biol.* **40** 917–30
- Li M-L, Li D-W, Hao-Li L and Lin M-S 2010 Ultrasonic Nakagami visualization of HIFU-induced thermal lesions *Ultrason. Symp. (IUS)* (IEEE) pp 2251–3
- Liao Y Y, Li C H, Tsui P H, Chang C C, Kuo W H, Chang K J and Yeh C K 2012 Strain-compounding technique with ultrasound Nakagami imaging for distinguishing between benign and malignant breast tumors *Med. Phys.* **39** 2325–33
- Liu T, Yang X, Bruner D, Tridandapani S, Chen H, Henry S and Rossi P 2012 Ultrasound Nakagami imaging for noninvasive evaluation of vaginal fibrosis following radiotherapy for gynecologic malignancies *Med. Phys.* **39** 3948–9
- Lizzi F L, Feleppa E J, Astor M and Kalisz A 1997 Statistics of ultrasonic spectral parameters for prostate and liver examinations *IEEE Trans. Ultrason. Ferroelectr. Freq. Control* **44** 935–42
- Lizzi F L, Ostromogilsky M, Feleppa E J, Rorke M C and Yaremko M M 1987 Relationship of ultrasonic spectral parameters to features of tissue microstructure *IEEE Trans. Ultrason. Ferroelectr. Freq. Control* **34** 319–29
- Madsen E L et al 1999 Interlaboratory comparison of ultrasonic backscatter, attenuation, and speed measurements *J. Ultrasound Med.* **18** 615–31
- Madsen E L, Hobson M A, Shi H, Varghese T and Frank G R 2005 Tissue-mimicking agar/gelatin materials for use in heterogeneous elastography phantoms *Phys. Med. Biol.* **50** 5597–618
- Mamou J and Oelze M L 2013 *Quantitative Ultrasound in Soft Tissues* (Berlin: Springer)
- Miller J G, Perez J E and Sobel B E 1985 Ultrasonic characterization of myocardium *Prog. Cardiovasc. Diseases* **28** 85–110
- Milunski M R, Mohr G A, Perez J E, Vered Z, Wear K A, Gessler C J, Sobel B E, Miller J G and Wickline S A 1989 Ultrasonic tissue characterization with integrated backscatter—acute myocardial ischemia, reperfusion, and stunned myocardium in patients *Circulation* **80** 491–503
- Mimbs J W, Bauwens D, Cohen R D, Odonnell M, Miller J G and Sobel B E 1981 Effects of myocardial ischemia on quantitative ultrasonic backscatter and identification of responsible determinants *Circ. Res.* **49** 89–96
- Molthen R C, Shankar P M, Reid J M, Forsberg F, Halpern E J, Piccoli C W and Goldberg B B 1998 Comparisons of the Rayleigh and K-distribution models using *in vivo* breast and liver tissue *Ultrasound Med. Biol.* **24** 93–100
- Montaldo G, Tanter M, Bercoff J, Benech N and Fink M 2009 Coherent plane-wave compounding for very high frame rate ultrasonography and transient elastography *IEEE Trans. Ultrason. Ferroelectr. Freq. Control* **56** 489–506
- Nakagami M 1960 The m-distribution—a general formula of intensity distribution of rapid fading *Statistical Method of Radio Wave Propagation* (Oxford: Pergamon) pp 3–36
- Nillesen M M, Lopata R G P, Gerrits I H, Kapusta L, Thijssen J M and de Korte C L 2008 Modeling envelope statistics of blood and myocardium for segmentation of echocardiographic images *Ultrasound Med. Biol.* **34** 674–80
- Oelze M L, Zachary J F and O'Brien W D Jr 2002 Characterization of tissue microstructure using ultrasonic backscatter: theory and technique for optimization using a Gaussian form factor *J. Acoust. Soc. Am.* **112** 1202–11
- Ophir J, Alam S K, Garra B, Kallel F, Konofagou E, Krouskop T and Varghese T 1999 Elastography: ultrasonic estimation and imaging of the elastic properties of tissues *Proc. Inst. Mech. Eng. H* **213** 203–33
- Ophir J, Cespedes I, Garra B, Ponnekanti H, Huang Y and Maklad N 1996 Elastography: ultrasonic imaging of tissue strain and elastic modulus *in vivo Eur. J. Ultrasound* **3** 49–70
- Papp J 2011 *Quality Management in the Imaging Sciences* (St Louis, MO: Mosby)
- Rangraz P, Behnam H and Tavakkoli J 2014 Nakagami imaging for detecting thermal lesions induced by high-intensity focused ultrasound in tissue *Proc. Inst. Mech. Eng. H* **228** 19–26
- Salomon G, Köllerman J, Thederan I, Chun F K H, Budäus L, Schlomm T, Isbarn H, Heinzer H, Huland H and Graefen M 2008 Evaluation of prostate cancer detection with ultrasound real-time

- elastography: a comparison with step section pathological analysis after radical prostatectomy *Eur. Urol.* **54** 1354–62
- Sandrin L, Fourquet B, Hasquenoph J M, Yon S, Fournier C, Mal F, Christidis C, Ziou M, Poulet B, Kazemi F, Beaugrand M and Palau R 2003 Transient elastography: a new noninvasive method for assessment of hepatic fibrosis *Ultrasound Med. Biol.* **29** 1705–13
- Shankar P M 1995 A model for ultrasonic scattering from tissues based on the K-distribution *Phys. Med. Biol.* **40** 1633–49
- Shankar P M 2000 A general statistical model for ultrasonic backscattering from tissues *IEEE Trans. Ultrason. Ferroelectr. Freq. Control* **47** 727–36
- Shankar P M, Dumane V A, Piccoli C W, Reid J M, Forsberg F and Goldberg B B 2002 Classification of breast masses in ultrasonic B-MODE images using a compounding technique in the Nakagami distribution domain *Ultrasound Med. Biol.* **28** 1295–300
- Shankar P M, Dumane V A, Reid J M, Genis V, Forsberg F, Piccoli C W and Goldberg B B 2001 Classification of ultrasonic B-mode images of breast masses using Nakagami distribution *IEEE Trans. Ultrason. Ferroelectr. Freq. Control* **48** 569–80
- Shankar P M, Reid J M, Ortega H, Piccoli C W and Goldberg B B 1993 Use of non-Rayleigh statistics for the identification of tumors in ultrasonic B-scans of the breast *IEEE Trans. Med. Imag.* **12** 687–92
- Shung K K 2005 *Diagnostic Ultrasound: Imaging and Blood Flow Measurements* (Boca Raton, FL: CRC)
- Szabo T L 2004 *Diagnostic Ultrasound Imaging* ed T L Szabo (Burlington: Academic) pp 243–95
- Thijssen J 2002 *Acoustical Imaging* ed M Halliwell and P T Wells (Berlin: Springer) pp 9–25
- Tsui P H and Chang C C 2007 Imaging local scatterer concentrations by the Nakagami statistical model *Ultrasound Med. Biol.* **33** 608–19
- Tsui P H, Hsu C W, Ho M C, Chen Y S, Lin J J, Chang C C and Chu C C 2010a Three-dimensional ultrasonic Nakagami imaging for tissue characterization *Phys. Med. Biol.* **55** 5849–66
- Tsui P H, Liao Y Y, Chang C C, Kuo W H, Chang K J and Yeh C K 2010b Classification of benign and malignant breast tumors by 2d analysis based on contour description and scatterer characterization *IEEE Trans. Med. Imag.* **29** 513–22
- Tsui P H, Huang C C, Sun L, Dailey S H and Shung K K 2011 Characterization of lamina propria and vocal muscle in human vocal fold tissue by ultrasound Nakagami imaging *Med. Phys.* **38** 2019–26
- Tsui P H and Tsai Y W 2015 Artifact reduction of ultrasound Nakagami imaging by combining multifocus image reconstruction and the noise-assisted correlation algorithm *Ultrason. Imag.* **37** 53–69
- Tsui P H and Wang S H 2004 The effect of transducer characteristics on the estimation of Nakagami parameter as a function of scatterer concentration *Ultrasound Med. Biol.* **30** 1345–53
- Tsui P H, Yeh C K, Chang C C and Liao Y Y 2008 Classification of breast masses by ultrasonic Nakagami imaging: a feasibility study *Phys. Med. Biol.* **53** 6027–44
- Tuthill T A, Sperry R H and Parker K J 1988 Deviations from Rayleigh statistics in ultrasonic speckle *Ultrason. Imag.* **10** 81–9
- Vered Z et al 1989 Ultrasound integrated backscatter tissue characterization of remote myocardial infarction in human subjects *J. Am. Coll. Cardiol.* **13** 84–91
- Wagner R F, Insana M F and Brown D G 1987 Statistical properties of radio-frequency and envelope-detected signals with applications to medical ultrasound *J. Opt. Soc. Am. A* **4** 910–22
- Wagner R F, Smith S W, Sandrik J M and Lopez H 1983 Statistics of speckle in ultrasound B-scans *IEEE Trans. Sonics Ultrason.* **30** 156–63
- Wells P N T and Liang H-D 2011 Medical ultrasound: imaging of soft tissue strain and elasticity *J. R. Soc. Interface* **8** 1521–49
- Yang X, Rossi P, Bruner D W, Tridandapani S, Shelton J and Liu T 2013 Noninvasive evaluation of vaginal fibrosis following radiotherapy for gynecologic malignancies: a feasibility study with ultrasound B-mode and Nakagami parameter imaging *Med. Phys.* **40** 022901
- Yu X and Lee W-N 2014 Characterization of the heart muscle anisotropy using ultrasound Nakagami imaging *IEEE Int. Ultrasonics Symp. (IUS) (3–6 September)* pp 2367–70
- Zagzebski J A, Chen J F, Dong F and Wilson T 1999 Intervening attenuation affects first-order statistical properties of ultrasound echo signals *IEEE Trans. Ultrason. Ferroelectr. Freq. Control* **46** 35–40